Kaguya Gamma-Ray Spectrometer
Ephemerides, Pointing & Geometry Data

T. H. Prettyman and N. Yamashita
Planetary Science Institute

Part of the Kaguya Gamma-Ray Spectrometer calibrated spectra data set
Version 1.0, 14-Jan-2020

Introduction

This document describes the methods used to calculate ephemerides, pointing, and geometry (EPG) data that accompany gamma-ray spectra acquired by the JAXA/SELENE (Kaguya) mission to the Moon. The data are part of the Kaguya gamma-ray spectrometer (KGRS) calibrated spectra archived at the Planetary Data System's Geosciences Node (Yamashita & Prettyman, 2020). The EPG data file includes the position and orientation of the spacecraft in a fixed lunar reference frame along with the solid angle subtended by the Moon. The EPG data are needed for the following analysis tasks: selection of valid data (e.g. entries that meet pointing and altitude criteria), geometry/altitude corrections, and mapping. The methods used to determine the parameters recorded in the data set are described here. The energy-dependent, efficiency-area product of KGRS accompanies the EPG data in the label file. A description of the methods used to calculate the efficiency-area product and experimental validation is described.

Identification of science data records

Science data were acquired by the Gamma Ray Spectrometer in 17s accumulation intervals. Spacecraft clock (SCLK) ticks (units of seconds) were provided for each of the 1,334,688 calibrated gamma-ray spectra included in the archive. SCLK refers to the time indices recorded by the spacecraft and included in the raw telemetry from which the calibrated spectra were derived. SCLK accompanies each entry in the EPG file and can be used as an unique identifier to associate the calibrated spectra with EPG data.

Time conversions

The SCLK ticks correspond to the end of each measurement interval. We converted SCLK to J2000 Epoch Time (ET) using the SPICE routine *scs2e*. SPICE is NASA's observation geometry information system available from the Navigation and Ancillary Information Facility (NAIF). The midpoint time for each measurement interval was determined by subtracting 8.5s from the epoch time. Midpoint epoch times were converted to Universal Coordinated Time (UTC) using *timout*. The leap second and SCLK kernels used for time conversions were respectively naif0012.tls and SEL_M_V01.TSC. All SPICE kernels specific to the SELENE mission were downloaded from JAXA's Data Archives and Transmission System (DARTS):

https://darts.isas.jaxa.jp/pub/spice/SELENE/kernels/

Generic kernels were downloaded from the NAIF/SPICE website:

https://naif.jpl.nasa.gov/naif/

Ephemerides and pointing data

Spacecraft position and orientation was determined at the midpoint epoch time for each measurement using SPICE in the Mean Earth/Polar Axis (ME) fixed lunar reference frame. The following kernels were used:

Leap second	naif0012.tls
SCLK	SEL_M_V01.TSC
Frames	SEL_V01.tf
	moon_080317.tf
	moon_assoc_me.tf
Instrument	SEL_LALT_V01.ti
Planetary constants	moon_pa_de421_1900-2050.bpc
	pck00010.tpc
Planetary ephemerides	de421.bsp
Spacecraft ephemerides	SEL_M_071020_090610_SGMH_02.BSP (lowest priority)
	SEL_M_071020_081226_SGMI_05.BSP (highest priority)
Spacecraft orientation	SEL_M_ALL_D_V02.BC

As no instrument kernel is available for the GRS, the instrument frame for the Kaguya laser altimeter (LALT) was used. For the relative position of the two instruments, see Fig. 4 of Kato et al. (2010). The +Z axis of the GRS points along the LALT boresight towards body center during science data acquisition. The GRS includes a high-purity germanium (HPGe) spectrometer and a bismuth germanate anticoincidence shield. Both have cylindrical geometry, with their axes of symmetry oriented in the Y-direction. For each measurement, the direction to body center was calculated in the LALT frame, represented as a vector, containing X-, Y-, and Z-direction cosines, USC, VSC, WSC, respectively. The +Z-cosine (WSC) can be used to identify measurements for which the spacecraft is pointing towards body center (e.g. Fig. 1a).

The SPICE-calculated position of the spacecraft in the ME frame, (X, Y, Z), distance from body center (D), and rectangular longitude and latitude (LON, LAT) are provided in the EPG file for each measurement (Fig. 1b). For 1552 measurements (0.1% of the calibrated data set), the pointing data could not be calculated. Position information was available for all of the calibrated spectra. An Invalid constant of -9 (negative nine) was set in cases where pointing data was unavailable for the corresponding calibrated gamma-ray spectrum.

Validation of the position data was carried out using Kaguya Lunar Magnetometer data archived at DARTS for which both SCLK and position were recorded (https://darts.isas.jaxa.jp/pub/pds3/sln-l-lmag-3-mag-ts-v1.0/). Differences between our SPICE-calculated positions and the positions recorded in the magnetometer data files were generally less than 400m, with rare deviations of about 1km. This is an acceptable uncertainty given the coarse (multi-km) spatial resolution of the GRS.

Solid angle calculations

The solid angle subtended by the Moon at the spacecraft was calculated using the Monte Carlo ray-tracing algorithm described by Prettyman (2017) and Prettyman et al. (2017, Supp. Text). The Moon was

represented by a shape model derived from a shape map in the ME fixed frame of DE421 derived from LRO/LOLA data (Smith, 2019). The LOLA point cloud converted to a polygonal shape model, which was decimated to maximize computational efficiency, while preserving topographic detail. The chord-length distribution of the shape model is shown in Fig. 2 along with a map of topography superimposed on shaded relief (Fig. 3).

The subsatellite distance in the body-center direction was also calculated using the shape model and is included in the EPG file.

The Monte Carlo propagated uncertainty in the solid angle was on average 0.5% with a population uncertainty of 0.08%. The statistical uncertainty is smaller than systematic variations in solid angle with orbital altitude. The propagated uncertainties are included along with the solid angle of the shape model and reference sphere in the EPG file.

A time series of solid angle, shown in Fig. 1c has an inverse variation with altitude. The equivalent altitude is that which gives the same solid angle for the reference sphere. This was calculated as

$$h_{eq} = R\left[1\Big/\sqrt{1-\left(1-\frac{\Omega}{2\pi}\right)^2}-1\right] \qquad \text{Eq. 1}$$

where Ω is the solid angle of the Moon calculated using the shape model and R is the radius of the reference sphere (1737.4 km). Since the Moon is nearly spherical, the equivalent altitude follows the distance from the spacecraft to the reference sphere in the direction of body center (cf. Figs. 1b and 1c). Consistent with the Dawn/GRaND data sets for Vesta and Ceres, equivalent altitude is provided along with solid angle in the EPG file.

Differences between the solid angle of the shape model and the reference sphere are shown in Fig. 4. A map of these differences formed using the entire data set is shown in Fig. 5. Larger deviations are observed when the spacecraft is closer to the Moon, which reflects the influence of topography on solid angle. The data-set average variations are relatively small compared to uncertainties in quantities derived from gamma-ray spectra. Thus, the spherical approximation is reasonable for many studies, particularly those that use the high-altitude portion of the data set. Shape-model derived solid angles would be of most benefit to studies using low altitude data acquired near the end of mission.

KGRS efficiency-area products

The KGRS consists of a large-volume, high purity germanium (HPGe) sensor, with an anticoincidence shield (ACS) consisting of an inorganic scintillator, bismuth germanate (BGO), and a plastic scintillator (Hasebe et al., 2008). The response of the KGRS to gamma rays was modeled using the general-purpose Monte Carlo radiation transport code MCNP. The arrangement of sensors and shielding materials is shown in Fig 6. Note that the BGO shield is thinner and open on the +Z side, which points towards body center during science data acquisition. The opening is covered by a thin plastic scintillator.

The composition and detailed geometry of the sensors and housing materials was determined from drawings provided by the KGRS team (priv. comm. N. Yamashita). The cryostat and PMT assemblies were approximated by cylindrical, aluminum endcaps shown in Fig. 6. The thickness of the endcaps was determined from laboratory angular measurements of a ^{60}Co point source. The full-energy efficiency for

the 1.333 MeV gamma-ray emitted by this source was measured for different angles about the X-axis, with the source positioned at different locations on the plane of symmetry (YZ) (see Fig. 3 of Kobayashi et al., 2010). This enabled attenuation measurements of the 1.333-MeV gamma ray. The ratio of the efficiency measured at $\pm 60^\circ$ to that measured with the source positioned on the +Z-axis, for which gamma rays can pass through the opening in the BGO/ACS. The ratio was about 0.2 for the cryostat side and 0.7 on the PMT side. With a linear attenuation coefficient of aluminum (0.144 cm^{-1}), this gives roughly 5-cm and 2-cm, respectively, for the equivalent thickness (Y-axis dimension) of the cryostat and PMT assemblies (as shown in Fig. 6a).

The geometric simplification of the cryostat and PMT assembly is justified based on experience modeling the sensor shielding configuration for other sensors and radiation detection systems. The inclusion of fine detail for passive components outside the sensor assembly is not required for estimates of azimuthally averaged efficiencies. The use of a simplified geometry with experimentally derived dimensions eliminated much of the guesswork needed to transfer the available 2D line drawings of the cryostat and PMT assemblies into a functional and efficient geometry for radiation transport.

The full-energy (photopeak), gamma-ray efficiency of the HPGe sensor was determined using the Pulse Height Light (PHL) anticoincidence tally in MCNPX 2.7, for which the active sensor components respond to the deposition of energy by secondary electrons. The tally was specified such that any energy deposition in the BGO or plastic scintillator resulted in a rejected event. This approach enabled calculation of the full-energy efficiency as well as the single- and double-escape efficiencies.

The full-energy efficiency was calculated as a function of gamma-ray energy for two cases: 1) a parallel beam of gamma rays traveling in the -Z direction; 2) gamma rays emitted from the lunar surface, with the spacecraft at an altitude of 100 km, the approximate mean altitude during the first part of the mission (Fig. 1). In the latter case, the emission distribution (angular current) was modeled as linear in the cosine of the emission angle and propagated to the detector. Linearly anisotropic emission is a reasonable approximation for gamma rays produced by nuclear reactions and is strictly valid for uncollided gamma rays made by the decay of radioelements in a homogeneous regolith (e.g. Prettyman et al., 2015). In both cases, a current source, with gamma rays crossing through a disk bounding the KGRS on the +Z, was modeled (e.g. Prettyman et al., 2019). The average score (probability of the gamma ray depositing full energy in the HPGe sensor per source particle) was multiplied by the area of the disk to determine the efficiency-area product (εA).

Results of the simulation are plotted in Fig. 7. The trends can be fitted by a polynomial:

$$\log\left(\varepsilon A\right) = \sum_{i=0}^{4} c_i x^i \ ,$$

where E is the energy of the gamma ray and $x = \log\left(E\right)$. The polynomial coefficients c_i are listed in Table 1 for each case. The shape of the response function depends on several factors, including attenuation by shielding materials and the projected area of the HPGe crystal. The efficiency of the -Z parallel beam illumination is relatively high for low-energy gamma rays, which experience minimal attenuation passing through the opening in the ACS/BGO. At high energies, the projected area of the HPGe crystal limits the detection efficiency. For the lunar case, incidence angles with higher projected

areas and longer chord lengths through the detector are sampled, resulting in higher efficiencies at high energy.

Kobayashi et al. (2010) measured the full-energy efficiency of KGRS at 1.333 MeV using a ^{60}Co standard source with known activity. They reported a total efficiency (ratio of particles emitted to particles detected) of ε_T = 0.08% $\pm$ 0.015% when the source was placed 30-cm from the center of the cannister in above the ACS opening (source positioned along the Z-axis). The efficiency-area product can be determined from the total efficiency by:

$$\varepsilon A = 4\pi \varepsilon_T r^2$$

Assuming $r \simeq$ 30 cm, this expression gives εA = 9 $\pm$ 2 cm^2, which is consistent with our calculations for parallel beam illumination (Fig. 7). This supports the validity of our calculations.

Table 1. Fitted polynomial coefficients, valid between 0.15- and 13-MeV.

i	Parallel beam (Z-axis)	Lunar surface (100 km altitude)
0	1.026	1.078
1	-0.6833	-0.5068
2	-0.05458	-0.337
3	-0.07617	-0.1843
4	-0.1874	0.0845

Acknowledgements

This work is supported by the NASA under Grant No. NNX16AG54G issued through the Planetary Data Archiving, Restoration, and Tools Program (PDART), Research Opportunities in Space and Earth Sciences (ROSES) 2015.

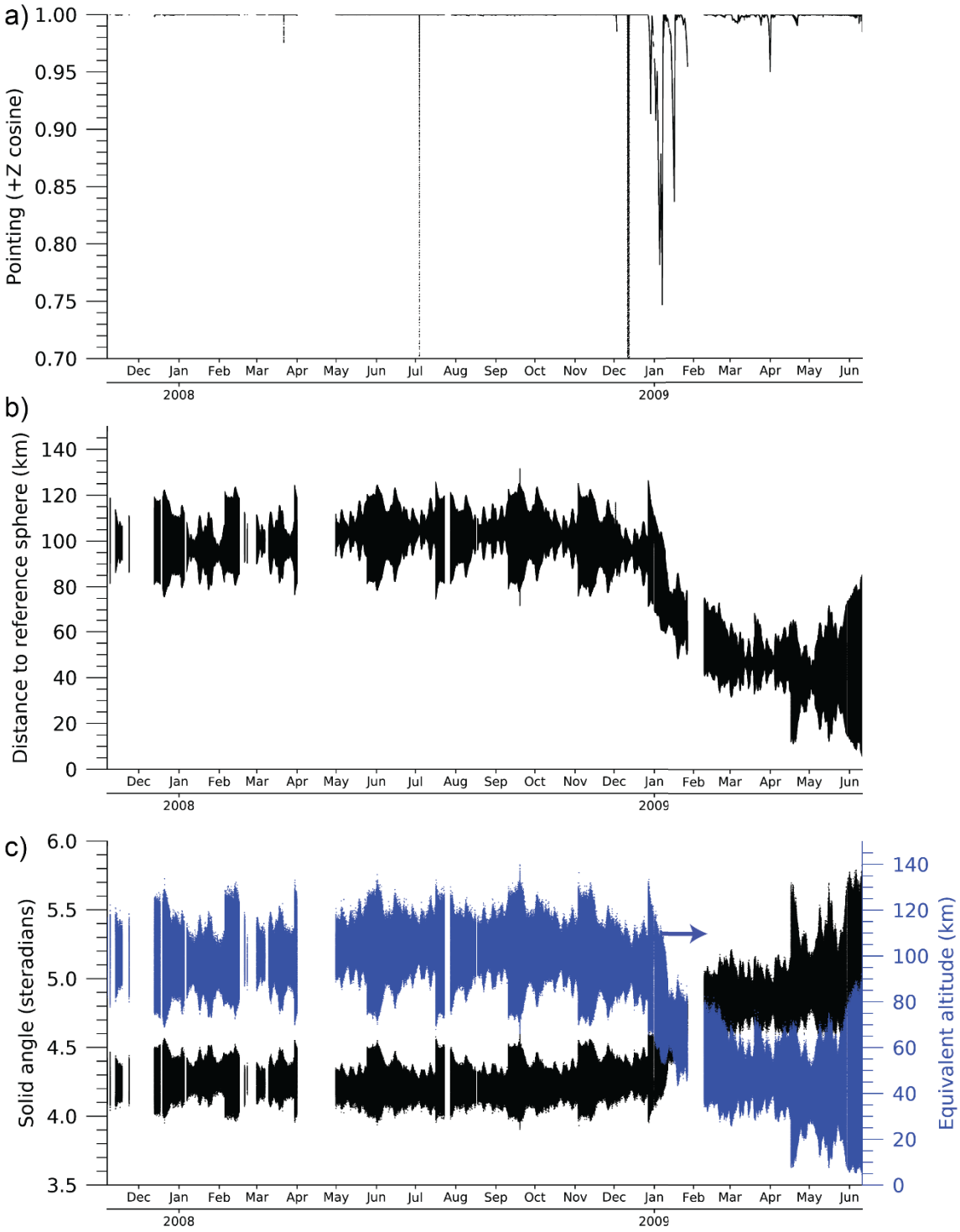

Figure 1. Calculated orbital parameters: a) Cosine of the angle between the +Z axis (instrument frame) and the direction to body center; b) Distance to body center offset by the radius of a reference sphere (1737.4 km); and c) solid angle subtended by the Moon represented by a shape model and equivalent altitude.

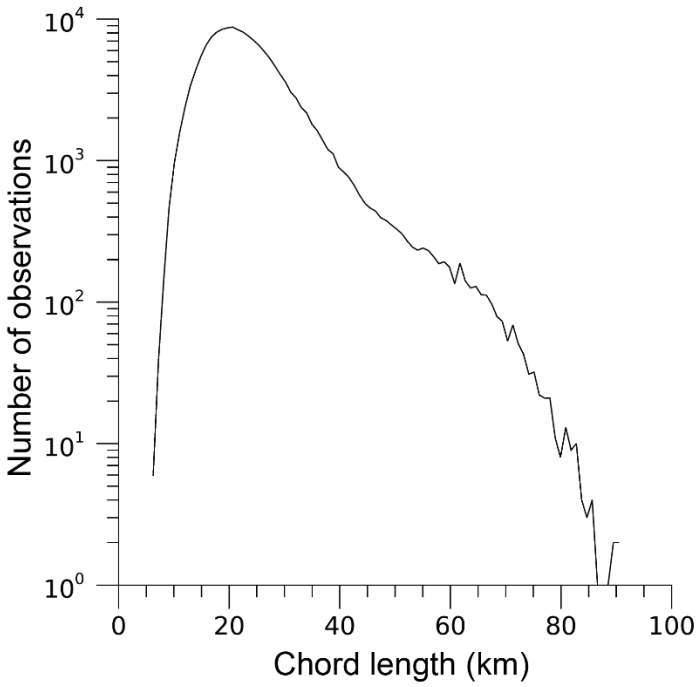

Figure 2. Histogram of chord lengths between the vertices of triangular plates that make up the shape model used to calculate solid angle and subsatellite distance. The shape model contained 624,256 plates with 3,190,017 vertices. The spatial scales sampled by the shape model are finer than the resolution of the GRS for most measurements. Spatial resolution varies approximately 1.5 × altitude.

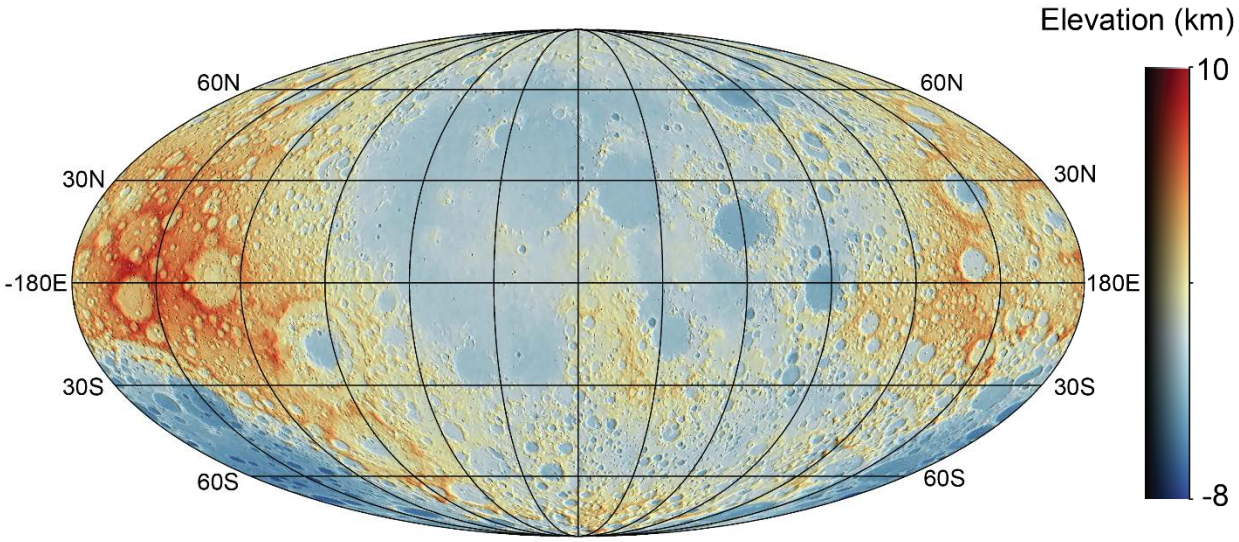

Figure 3. Map of topography superimposed on shaded relief determined from the shape model used to calculate solid angles. Elevation is relative to a reference sphere with 1737.4-km radius.

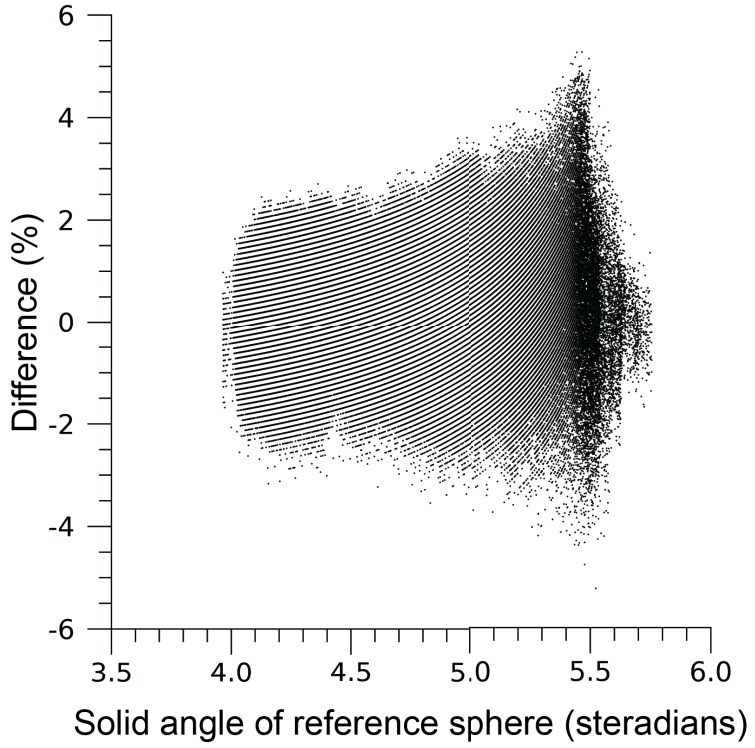

Figure 4. The percentage difference between the solid angle of the shape model and the reference sphere is shown for each measurement.

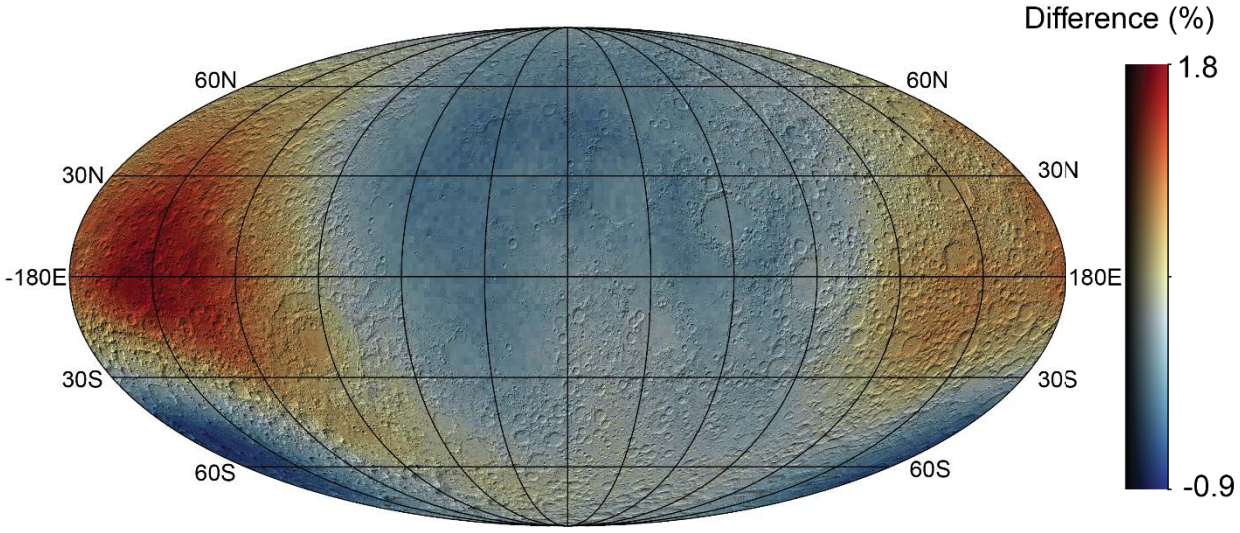

Figure 5. Map of the differences from Fig. 4 superimposed on shaded relief. The map was made by averaging the percentage differences between the solid angle of the shape model and the reference sphere on 2-degree cylindrical pixels. All measurement locations were used to form the map.

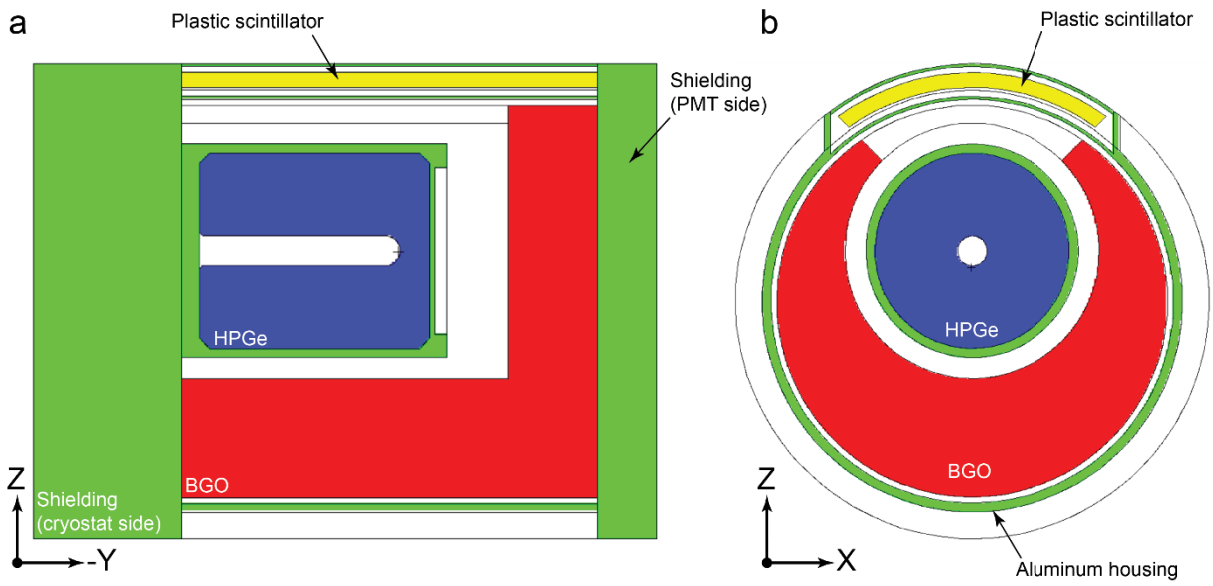

Figure 6. MCNP combinatorial geometry model of the KGRS, with cutaway views: a) YZ cut through the axis of symmetry (X); b) XY cut perpendicular to the axis of symmetry. Solid materials are indicated by colors: HPGe (blue); BGO (red); plastic scintillator (yellow); aluminum (green). The detailed geometry of the sensors and housing was modeled based on information provided by the KGRS team (priv. comm. N. Yamashita). Cylindrical aluminum regions approximate shielding by the cryostat and PMT assemblies. For reference, the HPGe crystal has a radius of 3.29 cm and a volume of 256.5 cm^3.

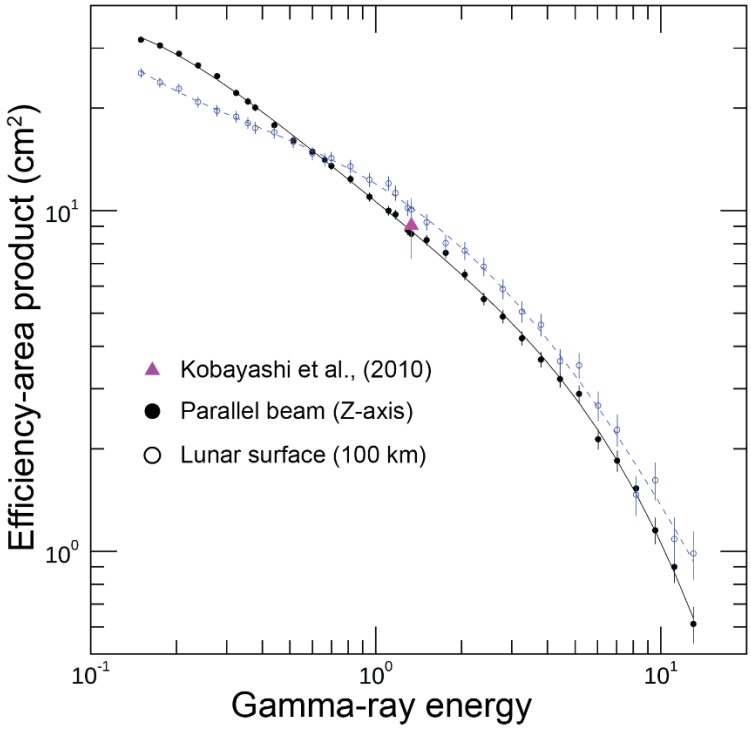

Figure 7. Efficiency-area products as a function of gamma-ray energy calculated by MCNP. The energy range sampled is 0.15- to 13-keV. The parallel beam calculation can be compared directly to a laboratory experiment with 1.333-MeV gamma rays Kobayashi et al. (2010).

References

Hasebe N., Shibamura E., Miyachi T., Takashima T., Kobayashi M., Okudaira O., Yamashita N., Kobayashi S., Ishizaki T., Sakurai K., Miyajima M., Fujii M., Narasaki K., Takai S., Tsurumi K., Kaneko H., Nakazawa M., Mori K., Gasnault O., Maurice S., d'Uston C., Reedy R.C. & Grande M. (2008) Gamma-ray spectrometer (GRS) for lunar polar orbiter SELENE. *Earth, Planets and Space*, **60**, 299-312.

Kato M., Sasaki S., Takizawa Y. & the Kaguya project team. (2010) The Kaguya Mission Overview. *Space Science Reviews*, **154**, 3-19.

Kobayashi S., Hasebe N., Shibamura E., Okudaira O., Kobayashi M., Yamashita N., Karouji Y., Hareyama M., Hayatsu K., d'Uston C., Maurice S., Gasnault O., Forni O., Diez B., Reedy R.C. & Kim K.J. (2010) Determining the Absolute Abundances of Natural Radioactive Elements on the Lunar Surface by the Kaguya Gamma-ray Spectrometer. *Space Science Reviews*, **154**, 193-218.

Prettyman T.H. (2017) Dawn GRaND Ephemeris, Pointing, and Geometry, V3. *DAWN-A-GRAND-3-RDR-CERES-COUNTS-V1.0, GRAND_EPG_DOC, NASA Planetary Data System*.

Prettyman T.H., Englert P.A.J. & Yamashita N. (2019) Neutron, gamma-ray, and X-ray spectroscopy: Theory and applications. Pp. 191-238 in: *Remote Compositional Analysis* (J.L. Bishop, J.F. Bell & J.E. Moersch, eds). Cambridge University Press, Cambridge.

Prettyman T.H., Yamashita N., Reedy R.C., McSween H.Y., Mittlefehldt D.W., Hendricks J.S. & Toplis M.J. (2015) Concentrations of potassium and thorium within Vesta's regolith. *Icarus*, **259**, 39-52.

Prettyman T.H., Yamashita N., Toplis M.J., McSween H.Y., Schorghofer N., Marchi S., Feldman W.C., Castillo-Rogez J., Forni O., Lawrence D.J., Ammannito E., Ehlmann B.L., Sizemore H.G., Joy S.P., Polanskey C.A., Rayman M.D., Raymond C.A. & Russell C.T. (2017) Extensive water ice within Ceres' aqueously altered regolith: Evidence from nuclear spectroscopy. *Science*, **355**, 55-59.

Smith D.E. (2019) Lunar Orbiter Laser Altimeter shape map. *LRO-L-LOLA-4-GDR-V1.0, LDEM_64_FLOAT, LOLA Planetary Data System data node*.

Yamashita N. & Prettyman T.H. (2020) Kaguya Gamma-Ray Spectrometer (KGRS): Calibrated Spectra Data Processing. *urn:nasa:pds:kaguya_grs_spectra:document:kgrs_calibrated_spectra, NASA Planetary Data System*.